Chapter 20
Ion Beam Analysis of GaN Surfaces and Interfaces

Joshua J. P. Cooper, Sam Frisone, Jiaheng He, Guanjie Cheng, Zhirong Zhang, and Rachel S. Goldman

1 Introduction

Wide-bandgap semiconductors such as GaN are promising for high-power electronics due to higher breakdown voltages and lower on-resistances compared to conventional Si-based devices [1, 2]. Vertical GaN p-i-n devices are expected to provide improved thermal management and reduced leakage current in comparison with their lateral counterparts [3, 4]. One of the main challenges in realizing vertical GaN p-i-n devices is the development of selective-area p-type doping techniques for lateral junctions. Despite its relatively high ionization energy of 145–245 meV [5, 6], Mg is the most effective p-type dopant for GaN to date [7, 8]. Strategies for selective-area Mg doping have included masked ion implantation and/or dopant diffusion; however, these approaches are limited to shallow junction formation and require high temperature annealing. A promising alternative involves a combination of selective-area etching followed by selective-area regrowth. For all selective p-type doping approaches, a detailed understanding of the influence of processing on the structure and properties of GaN surfaces and interfaces intended for use in vertical GaN p-i-n devices is needed.

To date, ion beam analysis techniques, including channeling Rutherford backscattering spectrometry (RBS/c) and elastic recoil detection analysis (ERDA) have been used to quantitatively determine composition, uniformity, impurity, and elemental depth profiles of major, minor, and trace elements in group III-V nitrides [9]. For example, RBS/c studies of heteroepitaxial GaN on sapphire [10–16], bulk GaN [17, 18], and implanted GaN [17, 19] have revealed χ_{min} values ranging from

J. J. P. Cooper · S. Frisone · J. He · G. Cheng · R. S. Goldman (✉)
University of Michigan, Ann Arbor, MI, USA
e-mail: rsgold@umich.edu

Z. Zhang
University of California Berkeley, Berkeley, CA, USA

I. C. Kizilyalli et al. (eds.), *Gallium Nitride and Related Materials*, The Materials Research Society Series, https://doi.org/10.1007/978-3-031-83056-3_20

1.2% to 4%; however, RBS/c studies of homoepitaxial GaN have not been reported. ERDA studies to date are limited to Mg-implanted GaN, revealing a Mg-induced increase in sub-surface [H] [17].

Therefore, in this chapter, we present new understanding of relationships between structure, chemistry, and electronic states at GaN surfaces and interfaces intended for use in vertical GaN p-i-n devices. In particular, we present investigations of depth-dependent crystallinity, atomic displacements, impurity incorporation, and electronic states using ion beam analysis techniques in conjunction with chemical and electronic characterization methods. First, we describe the ion beam analysis and chemical and electronic characterization methods, including Rutherford backscattering spectrometry (RBS), ERDA, and cathodoluminescence (CL) spectroscopy. Next, we describe investigations of surface treatments for selective-area regrowth of GaN substrates and regrown epitaxial GaN layers. The subsequent sections of the chapter focus on p-doped GaN layers prepared by Mg implantation and Mg/N co-implantation plus gyrotron annealing and electric field-assisted Mg diffusion. In the final section of the chapter, we compare and contrast the GaN surfaces and interfaces prepared by epitaxy/etching/regrowth, Mg ion implantation plus gyrotron annealing, and electric field-assisted Mg diffusion, suggesting promising avenues for future investigations.

2 Methods

In this section, we describe the methods used to examine the depth-dependent crystallinity, atomic displacements, impurity incorporation, and electronic states. First, we describe several RBS-based approaches including 2D planar channeling maps, as well as profiles of angular yields, channeling yields, and random yields, which are used together to examine depth-dependent crystallinity and atomic displacements. In addition, we describe ERDA, which is used to determine the depth-profile of [H]. Both RBS/c and ERDA were conducted using a 1.7 MV National Electrostatic Corporation tandem ion accelerator equipped with a fully-automated five-axis goniometer, with key details provided in Table 20.1, as described by Cooper et al. [20]. We also describe CL spectroscopy used to probe the depth-dependent electronic states associated with both Mg dopants and unintentional impurities at GaN surfaces and regrown interfaces. The CL spectroscopy was performed in a TESCAN RISE scanning electron microscope (SEM) equipped with a Gatan MonoCL4 detector [21, 22].

2.1 Channeling Rutherford Backscattering Spectrometry

Ion channeling is the focusing effect that occurs when a well-collimated beam of charged particles impinges upon a crystal in a direction of high atomic symmetry.

Table 20.1 Tabulated parameters for Rutherford Backscattering Spectrometry (RBS) and Elastic Recoil Detection Analysis (ERDA) measurements including incident particle, incident ion beam energy, incident ion beam angle (relative to surface normal), detector angle (relative to incident beam direction), and detected species

Experiment	Incident ion	Incident ion beam energy (MeV)	Incident beam angle (°)	Detector angle (°)	Detected species
RBS	H^+	1.5	0	160	Ga, N
RBS	He^{2+}	2.5	70	170	Ga, N
ERDA	He^{2+}	2.5	70	30	H

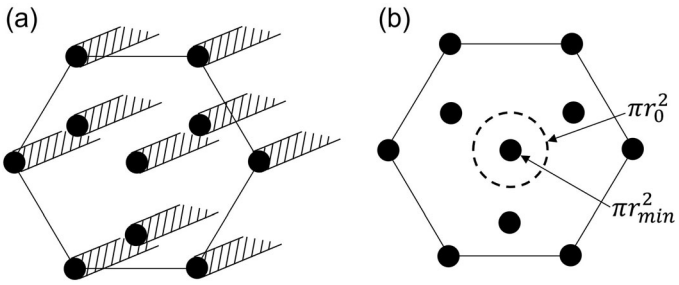

Fig. 20.1 (**a**) Schematic illustration of primitive cell for hexagonal close-packed crystal, with black circles representing atoms, hashed regions representing a column of atoms with radius $r_{\min}$, and the remaining white spaces representing ion channels with radius r_0. (**b**) Within $\pi r^2{}_0$ of each column of atoms, particles channel only for $r > r_{\min}$. Thus, the fraction channeled is $\frac{r_0^2 - r_{\min}^2}{r_0^2}$

As illustrated in Fig. 20.1a, when an ion beam is directly aligned along a crystallographic direction, the ions are steered by small-angle scattering collisions between rows and planes of atoms. As shown in Fig. 20.1b, the fraction of ions that are channeled is estimated as

$$f_{\text{channel}} = \frac{\pi r_0^2 - \pi r_{\min}^2}{\pi r_0^2} \tag{20.1}$$

where $r_{\min}$ is the atomic radius and r_0 is the radius of the ion channel surrounding the atom.

In the vicinity of the atomic row, the incident particles experience fewer close-encounters with atoms outside a small region surrounding the atomic rows, resulting in a reduced backscattered yield. In contrast, in the vicinity of atomic displacements, a fraction of the incident particles is de-channeled, leading to an increased probability for close-encounter collisions, resulting in an increased backscattered yield.

The fraction of ions that are not channeled is equivalent to the so-called minimum yield

Table 20.2 Structural and electronic properties of as-grown and etched GaN surfaces: ratios of channeling to random Rutherford backscattering spectrometry (RBS) yields summed over the top 100 nm, the so-called minimum yield, χ_{min}; fraction of displaced Ga, N_d/N; minimum yield from angular yield scans, Y_{min}; half-angle at half-minimum of angular yield scans, $\psi_{1/2}$ (°); lateral displacement of Ga atoms, r_x (nm); near band edge cathodoluminescence (NBE CL) emission intensity normalized to the emission of the as-grown GaN; Schottky barrier heights (SBH, eV); and ideality factors. For this analysis, χ_0 and ψ_0 are defined as the χ_{min} and the $\psi_{1/2}$ of the as-grown GaN

Surface	χ_{min}	N_d/N	Ymin	$\psi_{1/2}$ (°)	r_x(nm)	NBE CL	SBH (eV)	Ideality factor, n
as-grown	0.010	–	0.02	0.51	0.007	I_0	1.11	1.07
TBCl	0.011	0.002	0.02	0.51	0.007	$0.80I_0$	1.11	1.12
ICP	0.012	0.003	0.03	0.48	0.007	$0.25I_0$	0.66	1.79
ICP + TBCl	0.010	0.000	0.02	0.49	0.007	$0.54I_0$	0.96	1.18

$$\chi_{\text{min}} = 1 - f_{\text{channel}} = \frac{r_{\text{min}}^2}{r_0^2} \tag{20.2}$$

The minimum yield, χ_{min}, is often defined as the ratio of the "channeling" yield to the "random" yield. The "channeling" yield is provided by the RBS spectra collected along the channel axis, and the "random" yield is obtained by rotating the goniometer in θ and ϕ about the channel axis. The fraction of displaced Ga atoms over the depths of interest, N_d/N, is estimated via a comparison of the minimum yields of the processed GaN layers with that of a high-quality GaN substrate, as follows:

$$\frac{N_d}{N} = \frac{\chi_{\text{min}} - \chi_0}{1 - \chi_0} \tag{20.3}$$

where N is the Ga atomic density of the crystal and χ_0 is the minimum yield for a high-quality GaN substrate standard [23]. In this work, we use the as-grown GaN listed in Table 20.2 as the standard.

Another indication of the crystalline quality is the average displacement of the atoms, r_x, given by:

$$\psi_{1/2}/\psi_0 = \left(\ln\left[(Ca/r_x)^2 + 1\right]\right) / \left(\ln\left[(Ca/\rho)^2 + 1\right]\right) \tag{20.4}$$

where $C^2 = 3$, the Thomas-Fermi Screening radius is $a = 0.099$ Å, the thermal vibration amplitude is $\rho = 0.0620$ Å [24–27], and $\psi_{1/2}$ and ψ_0 are the half-angle at half-depths from angular yield scans for the processed GaN films and that of a high-quality GaN substrate standard, respectively. The as-grown GaN listed in Table 20.2 is also utilized as the standard for ψ_0.

To obtain $\psi_{1/2}$ and ψ_0, the angular-dependence of RBS yields (so-called "angular yield scans") were measured at ±3° about the $[11\bar{2}0]$ and $[1\bar{1}00]$ directions. The half-angle at half depth is determined from the width of the "well" at the half-depth

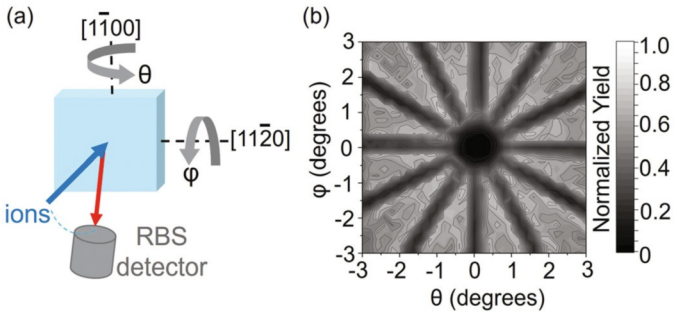

Fig. 20.2 (**a**) Illustration of Rutherford backscattering spectrometry (RBS): He or H ions (blue) are initially incident upon the GaN sample, and backscattered ions (red) are collected by a silicon surface-barrier detector. The automated ϕ-tilts (about the $[11\bar{2}0]$ axis) and θ-rotations (about the $[1\bar{1}00]$ axis), controlled by a five-axis goniometer, are also shown. (**b**) Normalized (0001) planar RBS channeling map, with yields integrated over the top 100 nm

of the normalized angular scans. In general, smaller values of $\psi_{1/2}$ correspond to larger values of the lateral atomic displacements, r_x.

For these experiments, the samples are mounted with copper tape onto the stage of a five-axis goniometer with computer control of polar (θ) and azimuthal (ϕ) rotations, as illustrated in Fig. 20.2a. Preliminary alignment to the sample surface normal is achieved using a laser that is coaxial with the incident ion beam.

Following sample surface alignment, a 2D planar scan is performed using the θ- and ϕ-ranges of $\pm 4°$ with a step size of 0.4°. The θ and ϕ values are adjusted so that the minimum yield was set at $\theta = 0$ and $\phi = 0$. Next a high resolution 2D planar scan is performed with θ- and ϕ-ranges of $\pm 3°$ with a step size of 0.2°, as shown in Fig. 20.2b for the [0001] channel of GaN. For the "random" spectra, the goniometer is set to 5° in ϕ away from the channel axis, and the backscattered signal is collected while the goniometer is rotated in θ (i.e., "rocked") from -5 to $+5°$ about the channel axis, in steps of 0.2°. Both the channeling and random yield profiles are collected using a silicon surface barrier detector equipped with an amplification system and multichannel analyzer which bins the signal into "channels" that are linearly proportional to the particle energy.

2.2 *Elastic Recoil Detection Analysis*

ERDA is a complementary ion beam analysis technique that enables quantitative analysis of light elements—in this case, it is used to probe the depth dependence of [H]. For ERDA, 2.5 MeV α particles are incident on the GaN at 70° to the surface normal, and recoiled H atoms are detected by a Si surface-barrier detector (the ERDA detector) located at 30° with respect to the incident beam. To filter out

scattered α particles, a 12.7 μm thick Kapton polyimide sheet is placed in front of the ERDA detector [28, 29]. Meanwhile, backscattered α particles are collected with another Si surface-barrier detector (the RBS detector) situated at 170° with respect to the incident ion direction.

For both RBS and ERDA, the yield of detected particles is given by:

$$Y = \sigma_i(\theta) \cdot \Omega \cdot Q \cdot N_s[i] \tag{20.5}$$

where Y is the yield, $\sigma_i(\theta)$ is the scattering cross-section at scattering angle θ, Ω is the detector solid angle, Q is the number of incident ions, and $N_s[i]$ is the areal density of target atoms i. The scattering cross-sections, $\sigma_i(\theta)$, for RBS of Ga and N were calculated using simulation of nuclear reaction analysis (SIMNRA) [30], and those for ERDA of H were taken from Ref. [31].

Due to the shallow angles of ion incidence and detection, accurate determination of the solid angles for the RBS detector (Ω_{RBS}) and ERDA detector (Ω_{ERDA}) is challenging. Instead, the ratio, $\Omega_{RBS}/\Omega_{ERDA}$, is determined using a target with known dimensions and [H] concentration, namely, a 1.5 cm × 1.5 cm sized Kapton sheet. Given the N_s value for Kapton, and the fact that $Q_{RBS} = Q_{ERDA}$ during simultaneous RBS and ERDA measurements, the measured Y_{RBS} and Y_{ERDA} for Kapton were used to determine $\Omega_{RBS}/\Omega_{ERDA} = 0.36$ for these experiments.

For the processed GaN films, simultaneous RBS and ERDA measurements were used to ensure $Q_{RBS} = Q_{ERDA}$. Using the measured value of Y_{RBS}, the known N_s for pure GaN, and the $\Omega_{RBS}/\Omega_{ERDA}$ ratio discussed above, $Q\Omega_{RBS}$ and $Q\Omega_{ERDA}$ were determined. Then, using the measured value of Y_{ERDA}, along with the reported $\sigma(\theta)$ for ERDA of H, N_s was computed, and [H] was determined for each measured GaN film.

2.3 Channel-to-Energy-to-Depth Conversion

For these ion beam analysis experiments, signals or "yields," consisting of counts vs channel, are obtained. Thus, to quantify depth profiles, both channel-to-energy and energy-to-depth conversions are needed. For example, for RBS, the channel-to-energy conversion is achieved by comparing the positions of Ga-edges for measured and simulated random yields from GaN. For ERDA, the positions of the H-edges for measured and simulated recoiled H yields from Kapton are compared. In both cases, the measured yield vs channel is fit to the simulated yield vs channel obtained using the SIMNRA code [30], with fitting parameters including the number of particles × Ω, detector resolution, and energy per channel, as described in Fig. 20.3a.

For the energy-to-depth conversion, the energy lost to collisions within the solid is considered, as illustrated in the inset in Fig. 20.3b. At a depth x, the energy of emitted ions is estimated as:

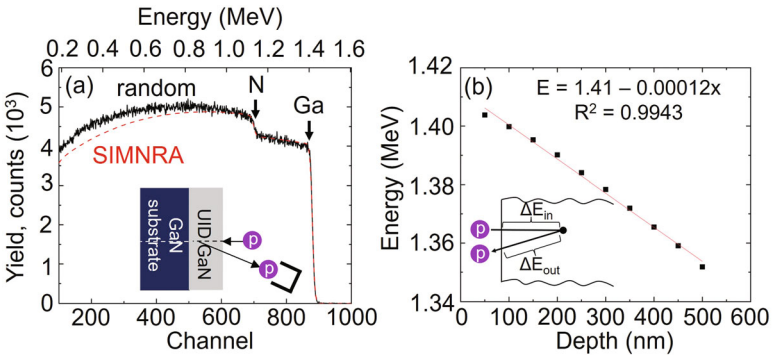

Fig. 20.3 (**a**) Plot of measured (black) and SIMNRA computed (red) "random" Rutherford backscattering spectrometry (RBS) yield vs channel, for example, UID-GaN. The best-fit to the data was determined by adjusting the number of particles (1.2×10^{11} protons·sr), detector resolution (23 keV), and energy per channel (1.58 keV/channel) within the SIMNRA simulation. (**b**) Backscattered energy vs depth, *E(x)*, from SIMNRA simulations of 1.5 MeV protons incident on GaN. An illustration of energy loss due to ion stopping power in a solid is shown as an inset. The depth-dependent energy loss allows for depth-sensitive measurements using a fixed ion energy

$$E(x) = E_0 - \int_0^x \frac{dE}{dx'}(E(x'), x')dx' \tag{20.6}$$

where the integral is the depth and energy-dependent ion stopping of the target sample. Differentiating this equation with respect to x gives:

$$\frac{dE}{dx} = -\epsilon(E) \tag{20.7}$$

where $\epsilon(E)$ is the energy-dependent stopping cross-section. Using SIMNRA [30], which incorporates stopping cross-section data from Ziegler [32], the emitted ion energy vs depth, *E(x)*, is computed, assuming equivalent channeling and random stopping powers [33]. In Fig. 20.3b, the backscattered energy vs depth, *E(x)*, is plotted for 1.5 MeV protons incident on GaN. Using a linear-least squares fit for *E (x)*, the RBS yield vs energy spectra is converted to yield vs depth. Similar approaches were used for the energy-to-depth conversions for the recoiled H yields in ERDA.

2.4 Cathodoluminescence Spectroscopy

CL spectra were collected in a Tescan RISE SEM equipped with a Gatan MonoCL4 Plus system. Within the SEM chamber, a parabolic mirror and light guide were used to collect emitted photons and couple them into an ex situ monochromator and

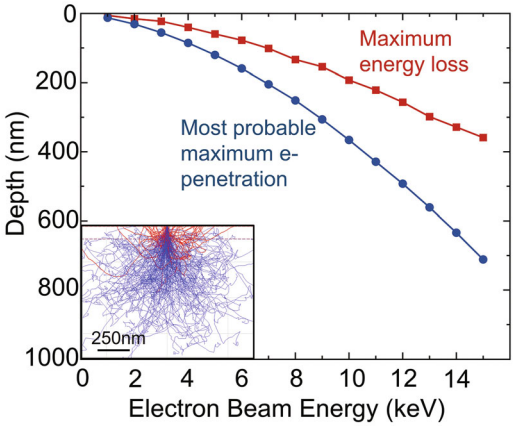

Fig. 20.4 CASINO simulations of electron trajectories in GaN: depths of maximum energy loss (red) and most probable electron penetration depth (blue) as a function of beam energy. For each beam energy, the simulated number of electrons vs maximum penetration depth was box-car smoothed and fit with a Gumbel distribution [35]. For the inset, red and blue electron trajectories indicate electrons which escape and do not escape the sample, respectively. Image processing of the corresponding electron trajectories was used to locate the highest density regions. (Reprinted from Ref. [21], with permission from Elsevier)

photomultiplier tube. The excitation depths for various electron-beam energies were estimated from CASINO Monte Carlo simulations of electron trajectories in GaN [34], as shown in Fig. 20.4. The average of the depths of maximum energy loss and most probable electron penetration was used to select appropriate beam energies (typically 5–10 keV) to preferentially probe the surfaces and buried interfaces. The electron beam spot size and current were selected to maintain power density at <0.34 W/cm^2. During electron beam scanning over 40×40 μm^2 regions, room temperature CL spectra were collected in the range 300–750 nm (4.12–1.65 eV) using a 50 nm blaze diffraction grating.

2.5 Schottky Barrier Height Measurements

In preparation for measurements of Schottky barrier heights, the GaN surfaces were etched with 1:1 HCl:HF for 60 s. Diodes with 80 μm diameter were prepared by e-beam evaporation of 20 nm/50 nm Ni/Au through a shadow mask onto the etched surfaces, followed by deposition of 20 nm/200 nm/20 nm/50 nm Ti/Al/Ni/Au layers on the backside of the GaN substrates. I–V measurements were performed at room temperature using a Keithley Model 4200 Semiconductor Characterization System, and the Schottky barrier heights and ideality factors were extracted from the forward-bias data.

3 Results and Discussion

3.1 *Epitaxy, Etching, and Regrowth*

In this section, we present investigations of GaN structures prepared by epitaxy, etching, and regrowth. In particular, the influence of ambient exposure and/or chlorine-based etching approaches on the structure and properties of GaN surfaces and regrown layers are described. Following a review of recent etching/regrowth approaches toward vertical GaN devices, we describe the sequence of metalorganic-vapor-phase epitaxy (MOVPE), chlorine-based chemical etching, and regrowth used to prepare the structures. We then present data from RBS/c, ERDA, CL, and secondary ion mass spectrometry (SIMS).

Selective-area etching and regrowth have emerged as a promising approach for vertical GaN devices on various substrates. For GaN substrates, both vertical p-n and n-p GaN devices have been demonstrated [36–39]. To date, the limited performance of vertical GaN devices, including low breakdown voltages and high leakage currents, has been attributed to imperfections at the regrowth interface [40, 41]. It has been suggested that the regrowth interface disrupts the GaN stoichiometry, resulting in interfacial N vacancies [42]. In the vicinity of the regrowth interfaces, C, O, and Si concentrations have been quantified [42, 43], and strategies to reduce their concentrations have been explored. For example, annealing in NH_3 has been shown to reduce the surface/interface concentrations of C and O [44, 45]. To reduce interfacial Si concentrations, Cl-based plasma and dry etching [46], wet chemical etching, and UV-ozone cleaning [43, 45] have been utilized. However, the influence of these surface/interface treatments on the crystallinity and electronic states is just beginning to be explored [21, 47].

For these investigations, UID-GaN layers were grown on n-type GaN surfaces using MOVPE; they were subsequently processed with two chlorine-based etchants, tertiary-butyl chloride (TBCl), performed within the MOVPE system, and/or Cl_2/BCl_3 inductively coupled plasma (ICP), performed ex situ, as illustrated in

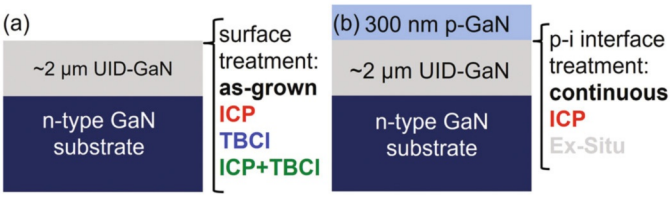

Fig. 20.5 GaN structures prepared by epitaxy, etching, and regrowth: (**a**) surface-treated UID-GaN layers grown on n-type GaN substrates, and (**b**) p-GaN layers (3×10^{19} cm^{-3}) grown on surface-treated UID-GaN layer structures on n-type GaN substrates. For (**a**), the surface treatments include ex situ inductively coupled plasma (ICP), in situ tertiary-butyl chloride (TBCl), and ex situ ICP etching followed by in situ TBCl exposure (ICP + TBCl), in comparison with as-grown UID-GaN (as-grown). For (**b**), the interface treatments include air exposure (ex situ) and ICP etching (ICP), in comparison with continuously grown layers (continuous)

Fig. 20.5a and b. For select samples, in situ and/or ex situ etchings were followed by MOVPE growth of a p-GaN layer, as illustrated in Fig. 20.5b. Additional discussion of TBCl etching is given in Chap. 12 of this book.

Our ion beam analysis studies reveal that the all in situ prepared GaN surfaces have the lowest fraction of displaced Ga atoms, the highest near band edge (NBE) CL emissions, and nearly ideal diode characteristics. Meanwhile, for the GaN p-i-n structures, the fraction of displaced Ga atoms, summed from the surface to the regrown p-i interface, is about >2× higher than those of the etched surfaces, presumably due to the displacement of Ga by Mg incorporation in the p-layers. In addition, the all in situ prepared GaN p-i-n structures have the highest donor-acceptor pair (DAP) CL emission. Interestingly, observation of yellow luminescence (YL) at the ex situ prepared regrown p-i interfaces is consistent with the recent hypothesis that YL is due to a surface state associated with air exposure [48].

3.1.1 Surface-Treated UID-GaN Layers

The [0001] channeling RBS spectra from an as-grown (black) GaN film as well as those from ICP (red), ICP + TBCl (green), and TBCl (blue) etched GaN films, are shown in Fig. 20.6a. In addition, the random RBS spectrum from the as-grown GaN is plotted (black dashed). In Fig. 20.6a, a high backscattered yield, with well-defined N- and Ga-edges, is apparent for the random spectrum, with significantly reduced yields for the channeling spectra, as expected for single crystals. The close-up view of the channeling spectra in Fig. 20.6b allows us to quantify changes in crystallinity, at specific depths, following etching.

To quantify the depth-dependent crystallinity, we consider the fractions of backscattered ions using the minimum yield, χ_{min}, defined as the ratio of the channeling yield to the random yield, summed over the depth of interest, in this case, the top 100 nm. As shown in Table 20.2, χ_{min} values of 0.01 are observed for both the as-grown and TBCl-etched GaN, suggesting a fraction of displaced Ga, $N_d/N < 0.002$. For the ICP-etched GaN, χ_{min} increases to 0.012, resulting in $N_d/N \approx 0.003$. Interestingly, a subsequent TBCl etch (i.e., "ICP + TBCl") reduces χ_{min} to 0.01, indicating $N_d/N < 0.002$ once again. Thus, the ICP etch disrupts the crystallinity of the GaN surface, but the damage may be recovered by TBCl etch.

The angular-dependence of the channeling RBS yields are shown in Fig. 20.7 for (a) $Y_{Ga}(\phi)$ (rotation about $[11\bar{2}0]$) and (b) $Y_{Ga}(\theta)$ (rotation about $[1\bar{1}00]$). $Y_{Ga}(\theta)$ and $Y_{Ga}(\phi)$ were collected from the top 100 nm of the ICP + TBCl etched, TBCl etched, ICP etched, and as-grown GaN films. For the as-grown GaN, the minimum yield, $Y_{min,Ga}$, illustrated as a dashed horizontal line in Fig. 20.7a, is apparent at $\theta = 0$, where the incident beam is aligned along the [0001] channel. For the as-grown GaN, the $Y_{min,Ga}$ values are essentially identical for $Y_{Ga}(\theta)$ and $Y_{Ga}(\phi)$. In addition, well-developed shoulders are apparent near the channel edges for $Y_{Ga}(\theta)$, but they are absent for $Y_{Ga}(\phi)$, presumably due to differences in flux focusing at the $(11\bar{2}0)$ and $(1\bar{1}00)$ surfaces [18, 49]. The presence of well-defined shoulders suggests a highly crystalline structure, as evidenced by the low values of χ_{min} and N_d/N in Table 20.2.

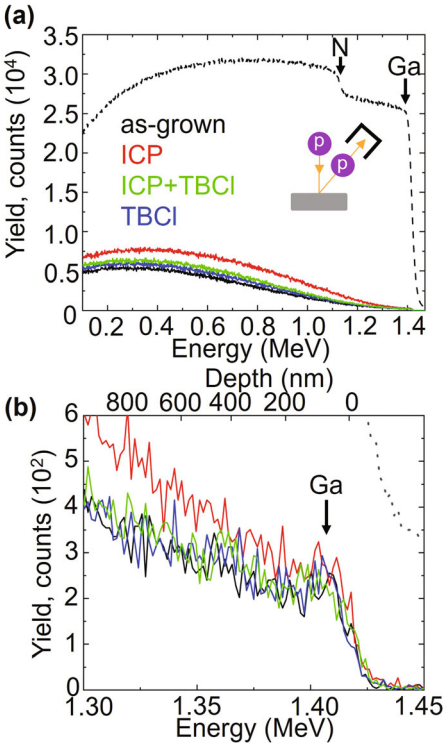

Fig. 20.6 (**a**) Random and channeling Rutherford backscattering spectrometry (RBS) yield vs backscattered particle energy for GaN following MOVPE growth (black), and post-growth surface treatments including inductively coupled plasma (ICP) etching (red), tertiary-butyl chloride (TBCl) etching (blue), and ICP + TBCl etching (green), with close-up view of RBS spectra in the vicinity of the surface in (**b**)

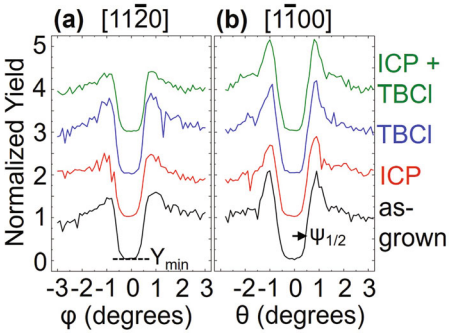

Fig. 20.7 Angular-dependence of the [0001] channeling Rutherford backscattering spectrometry (RBS/c) yields, rotated about the (**a**) $[11\bar{2}0]$ and (**b**) $[1\bar{1}00]$ axes. These angular yield scans were collected from the top 100 nm of the GaN following MOVPE growth (black), ICP etching (red), TBCl etching (blue), and ICP + TBCl etching (green). Example minimum yields, $Y_{\mathrm{min,Ga}}$, and half-width at half-depth, $\psi_{1/2}$, are illustrated by the dashed horizontal line in (a) and the horizontal arrow in (b), respectively

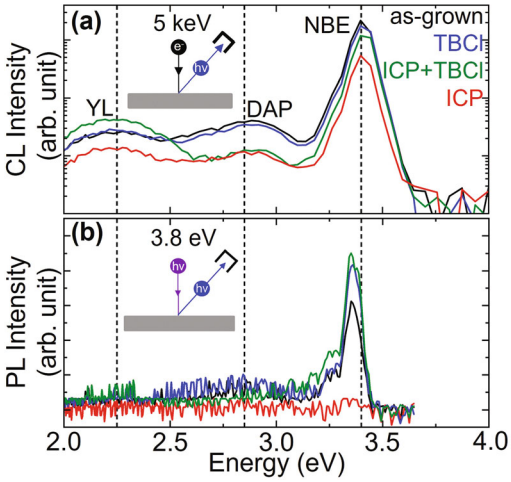

Fig. 20.8 (**a**) Cathodoluminescence (CL) and (**b**) photoluminescence (PL) spectra of MOVPE-grown UID-GaN (black), inductively coupled plasma (ICP) etched UID-GaN (red), tertiary-butyl chloride (TBCl) etched UID-GaN (blue), and ICP followed by TBCl etched UID-GaN (green). For the CL in (**a**), regions in the vicinity of the surfaces are probed using a beam energy of 5 keV. For the PL in (**b**), the incident laser energy was 3.8 eV. (b) is reproduced from Ref. 46, with permission from Elsevier

Finally, the half-width at half-depth, $\psi_{1/2}$, is illustrated with a horizontal arrow in Fig. 20.7b. As summarized in Table 20.2, $\psi_{1/2}$ values of 0.49 ± 0.02° are apparent for all of the GaN surfaces, consistent with earlier measurements of GaN [12, 15, 18]. The corresponding displacements of Ga atoms from the [0001] row, r_x, are 0.007 nm, similar to the thermal vibration amplitude.

We now consider the luminescence from the surface-treated UID-GaN layers, via the CL and photoluminescence (PL) spectra in Fig. 20.8a and b. Both the CL and PL spectra reveal NBE emissions at ≃3.4 eV. For the CL shown in Fig. 20.8, the intensity of NBE emission is highest for the as-grown UID-GaN and lowest for the ICP-etched GaN. Similarly, the NBE PL emission for the ICP-etched GaN is lowest, namely, it is quenched. CL emissions are also apparent at 2.85 eV and 2.2 eV, presumably due to impurity-related DAP and YL, respectively. It is interesting to note that for the all in situ prepared surfaces, as-grown and TBCl-etched, the NBE CL emissions are the highest, and the intensity of the DAP is higher than that of the YL. On the other hand, for those surfaces etched ex situ via ICP, the NBE CL emissions are reduced (with some recovery following TBCl etching) and the intensity of the YL exceeds that of the DAP. A quantitative comparison of the NBE CL intensities is listed in Table 20.2.

Finally, we compare the performance of Schottky barrier devices prepared with various GaN surface treatments, as listed in Table 20.2. For all cases, Ni/Au contacts were deposited on the GaN surfaces and current–voltage (I–V) characteristics were measured at room temperature. The Schottky barrier heights and ideality factors for each surface treatment are summarized in Table 20.2. For the as-grown and TBCl etched GaN surfaces, similar Schottky barrier heights (1.11 eV) and ideality factors

(~1.1) are apparent. In contrast, the ICP etch leads to the lowest Schottky barrier height (0.66 eV) and highest ideality factor (1.79), indicating non-ideal diode behavior, likely associated with the interfacial atomic displacements, i.e., increased N_d/N, discussed above. For the ICP + TBCl etch, the Schottky barrier height is increased to 0.96, with an ideality factor of 1.18. The nearly-ideal diode behavior for the ICP + TBCl-etched GaN diode correlates well with the decrease in atomic displacements, i.e., reduced N_d/N, discussed above.

3.1.2 GaN p-i-n Structures

Figure 20.9 presents [0001] channeling RBS spectra from the continuous (black), ex situ (gray), and ICP etched (red) GaN p-i-n structures, in comparison with a random RBS spectrum from a UID GaN layer prior to p-GaN growth. In Fig. 20.9a, a high backscattered yield, with well-defined N- and Ga-edges, is apparent for the random spectrum, with significantly reduced yields for the channeling spectra. To quantify

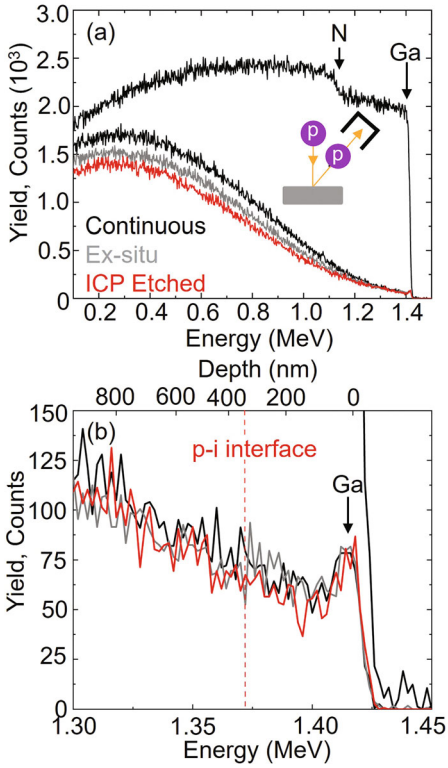

Fig. 20.9 (**a**) Random and channeling Rutherford backscattering spectrometry (RBS) yield vs backscattered particle energy for MOVPE-grown p-GaN layers grown on UID GaN layers, with close-up view of RBS spectra in the vicinity of the p-i interface in (**b**). The black, gray, and red spectra are data from the p-GaN grown on UID GaN without interruption (continuous), following air exposure and re-insertion into the MOVPE (ex situ), and following air exposure, ICP-etching, and re-insertion into the MOVPE (ICP etched). The position of the p-i interface is indicated by a vertical dashed line in (b)

Table 20.3 Structural and electronic properties of continuous, ex situ, and ICP-etched p-i-n GaN structures: ratios of channeling to random Rutherford backscattering spectrometry (RBS) yields summed over top 350 nm, the so-called minimum yield, χ_{min}; the fraction of displaced Ga, N_d/N; interfacial [Si] and [H]; interfacial cathodoluminescence (CL) emission intensities from Fig. 20.11b: yellow luminescence (YL), donor-acceptor pair (DAP), and near band edge (NBE) normalized to the CL emission of the continuous p-i-n GaN structure. For this analysis, χ_{min} and $\psi_{1/2}$ for the as-grown GaN from Table 20.2 are defined as χ_0 and $\psi_{1/2}$, respectively

p-i-n structure	χ_{min}	N_d/N	[Si] (10^{18} cm^{-3})	[H] (10^{20} cm^{-3})	YL	DAP	NBE
Continuous	0.016	0.007	0.1	2.2	I_0	I_0	I_0
Ex situ	0.017	0.008	1.1	1.8	$1.80I_0$	$0.86I_0$	$0.44I_0$
ICP	0.014	0.005	70	10	$2.98I_0$	$0.47I_0$	$1.11I_0$

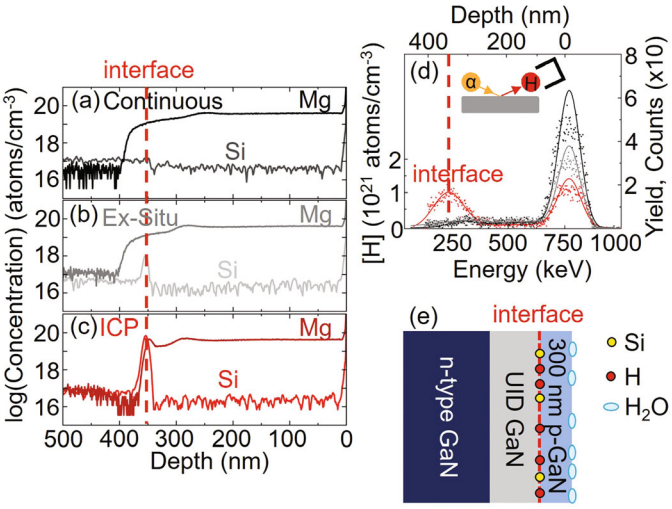

Fig. 20.10 Secondary ion mass spectrometry (SIMS) and elastic recoil detection analysis (ERDA) data: depth-dependence of [Mg] and [Si] from SIMS for (**a**) continuous (black), (**b**) ex situ (gray), and (**c**) ICP etched (red) GaN p-i-n structures. In (a)–(c), the dashed red line indicates the p-i interface. (**d**) Depth-dependence of [H] concentration from ERDA. (**e**) Illustration of ICP-etched GaN p-i-n structure with enhanced [H] and [Si] at the p-i interface

the depth-dependent crystallinity from the surface to the p-i interface, we compute χ_{min} summed over the top 350 nm, as illustrated by the vertical dashed line in Fig. 20.9b. The resulting χ_{min} and N_d/N values are listed in Table 20.3. For all of the GaN p-i-n structures, $\chi_{min} = 0.015 \pm 0.02$ with $N_d/N = 0.007 \pm 0.002$, indicating that any atomic displacements of Ga during air exposure and/or ICP etching were restored during the regrowth process.

The depth-dependence of the impurity concentrations were determined using a combination of SIMS and ERDA, as shown in Fig. 20.10, with the surface to bulk spanning from the right to the left. In Fig. 20.10, the SIMS data of (a) continuous,

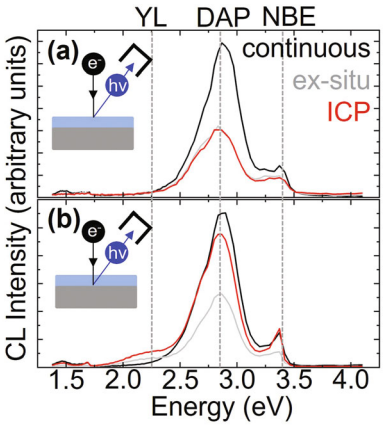

Fig. 20.11 Cathodoluminescence (CL) spectra from continuous (black), ex situ (gray), and ICP-etched (red) GaN p-i-n structures. To probe the surface and p-i interface, the CL spectra are generated with electron beam energies of (**a**) 5 keV and (**b**) 10 keV, respectively

(b) ex situ, and (c) ICP-etched GaN p-i-n structures, reveal similar depth-dependences of [Mg], with the highest [Mg] ($\simeq 5 \times 10^{19}/cm^3$) in the p-GaN layers, and the lowest [Mg] ($\leq 10^{17}/cm^3$) in the UID-GaN layers. The SIMS data also reveal similar depth-dependences of [Si], with the lowest [Si] ($\leq 10^{17}/cm^3$) in the p-GaN layers, and slightly higher [Si] ($\simeq 10^{17}/cm^3$) in the UID-GaN layers. In the vicinity of the p-i interface, indicated by the vertical red dashed line at the depth of 350 nm in Fig. 20.10a–c, the [Mg] monotonically decreases across the interface (from the surface to bulk) for (a) continuous and (b) ex situ p-i interfaces. However, for the ICP-etched p-i interface in Fig. 20.10c, an enhancement of [Mg] to $\simeq 4 \times 10^{20}/cm^3$ is apparent. It is interesting to note that enhancements of [Si] are also apparent at the ex situ and ICP-etched p-i interfaces in Fig. 20.10b and c, with peak concentrations of $10^{18}/cm^3$ and $\simeq 7 \times 10^{19}/cm^3$, respectively. Meanwhile, the depth-dependence of the [H] in Fig. 20.10d reveals ≃3–10 nm of surface H_2O for the continuous, ex situ, and ICP-etched GaN p-i-n structures. For all samples, [H] drops to $\simeq 10^{19}/cm^3$ within 280 nm of the surface, and a slight increase in [H] to $\simeq 10^{20}/cm^3$ at ≃300 nm depth is apparent. In addition, for the ICP-etched GaN p-i-n structure, an enhancement of [H] to $\geq 10^{21}/cm^3$ is apparent at the p-i interface. Thus, while air exposure leads to elevated [Si] at the p-i regrowth interface, ICP etching results in a further enhancement of [Si], as well as elevated [H] and [Mg], as illustrated in Fig. 20.10e.

We now consider the electronic properties of the surface and p-i interface for the continuous, ex situ, and ICP-etched GaN p-i-n structures. As shown in Fig. 20.11, CL spectra were generated with electron beam energies of (a) 5 keV and (b) 10 keV, which probe the surface and p-i interface, respectively. For the near-surface regions in Fig. 20.11a, the emissions observed at 2.85 eV and 3.4 eV are attributed to DAP and NBE emission, respectively. For the ex situ and ICP-etched GaN p-i-n

structures, the relative intensities of DAP and NBE are similar. Meanwhile, the continuous GaN p-i-n structure exhibits a higher DAP to NBE intensity ratio. For the p-i interface regions in Fig. 20.11b, the DAP to NBE intensity ratios for continuous and ex situ are essentially unchanged, while that of the ICP-etched structure has increased substantially. In addition, a new emission at 2.25 eV—the YL—is apparent. Interestingly, the intensity of the YL is highest at the buried p-i interface within the ICP-etched p-i-n structure, with an intermediate intensity at the buried p-i interface within the ex situ p-i-n structure. These findings are consistent with the attribution of YL to a surface state induced during air exposure [48]. A quantitative comparison of the CL emission intensities is provided in Table 20.3.

3.2 Ion Implantation and Gyrotron Annealing

In this section, we present investigations of GaN structures prepared by Mg implantation and Mg/N co-implantation, followed by gyrotron annealing. Following a brief review of gyrotron annealing and its potential impact on vertical GaN device technology, we describe the sequences of box implantation/co-implantation and gyrotron annealing used to prepare the structures. We then present RBS/c data, emphasizing the impact of the implantation and annealing processes on GaN crystallinity. More details of gyrotron annealing on Mg implanted GaN are reviewed in Chap. 14 of this book.

Due to the need for post-growth annealing to drive off passivating H from precursors used in GaN MOVPE [50, 51], ion implantation continues to be a viable alternative for vertical p-n devices [52, 53]. However, p-n device fabrication using ion implantation is limited to shallow junction formation, and requires both masking for lateral selectivity and high temperature annealing to resolve lattice damage. Recently, microwave annealing was proposed as a promising alternative due to its promise for lateral precision in shallow junction formation, without the need for ultra-high temperature annealing [54]. Specifically, a gyrotron microwave generator [55] enables radiative heating with an ultra-high temperature ramp rate (10,000 °C/s). Although PL studies suggest that gyrotron annealing of Mg implanted GaN has enabled substitutional incorporation of Mg, Mg_{Ga}, the limited doping efficiency was attributed to high concentrations of V_N generated during implantation [54, 56]. Aiming to mitigate the formation of V_N [57, 58], thereby increasing the maximum hole concentration, Mg/N co-implantation followed by gyrotron annealing was also explored [59, 60].

For these investigations, MOVPE-grown UID GaN layers were implanted with a three-step box-implant targeting depths/concentrations of 500 nm GaN with [Mg] = 1×10^{19} cm^{-3} and 250 nm GaN with [Mg] = [N] = 1×10^{19} cm^{-3}, as illustrated in Fig. 20.12 and Table 20.4. All ion implantations were performed at 7° tilt with 23° twist relative to the c-plane to prevent ion channeling. For a subset of the implanted GaN layers, gyrotron annealing was performed using 15 pulses at 1000 °C at a pressure of 4 MPa in N_2 gas [54, 59].

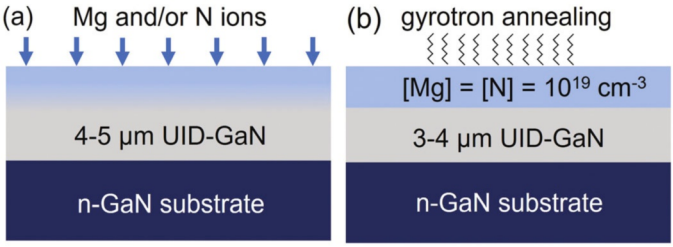

Fig. 20.12 Epitaxial UID GaN layers prepared with box implants, before and after gyrotron annealing: (**a**) Mg implantation or Mg/N co-implantation was achieved using 3-step box implants described in Table 20.4 and (**b**) following gyrotron annealing, the targeted structures consist of 500 nm GaN with [Mg] = 1×10^{19} cm^{-3} or 250 nm GaN with [Mg] = [N] = 1×10^{19} cm^{-3}

Table 20.4 Approach for box implantation of GaN with Mg or Mg + N, including targeted implanted species, depths, and concentrations. The ion energies and ion doses for each step are also provided

Species	Depth (nm)	[Mg] (10^{19} cm^{-3})	[N] (10^{19} cm^{-3})	Mg Ion Energy (keV)	Mg Ion Dose (10^{14} cm^{-2})	N Ion Energy (keV)	N Ion Dose (10^{14} cm^{-2})
Mg	500	1.0	N/A	–	–	–	–
				100	0.9	N/A	N/A
				200	1.3	N/A	N/A
				400	3.3	N/A	N/A
Mg, N	250	1.0	1.0	–	–	–	–
				100	0.9	90	0.7
				180	0.9	150	1.0
				270	3.0	240	3.0

The [0001] channeling RBS spectra for as-grown GaN (black), GaN following Mg implantation (cyan, dashed), and GaN following Mg implantation plus gyrotron annealing (cyan, solid) are shown in Fig. 20.13a and c. Similarly, the [0001] channeling RBS spectra for as-grown GaN, GaN following Mg/N co- implantation (magenta, dashed), and GaN following Mg/N co-implantation plus gyrotron annealing (magenta, solid) are shown in Fig. 20.13b and d. For both cases, RBS/c for the as-grown GaN is plotted in black, with dashed (solid) lines corresponding to random (channeling) spectra in Fig. 20.13a–d. In Fig. 20.13a and b, high backscattered yields, with well-defined N- and Ga-edges, are apparent for the random spectra, with significantly reduced yields for the channeling spectra, as expected for single crystals. The close-up views of the channeling spectra in Fig. 20.13c and d allow us to quantify changes in crystallinity, at specific depths, following implantation and implantation plus gyrotron annealing.

To quantify the depth-dependent crystallinity, we consider the fractions of backscattered ions using the minimum yield, χ_{min}, summed over the top 100 nm.

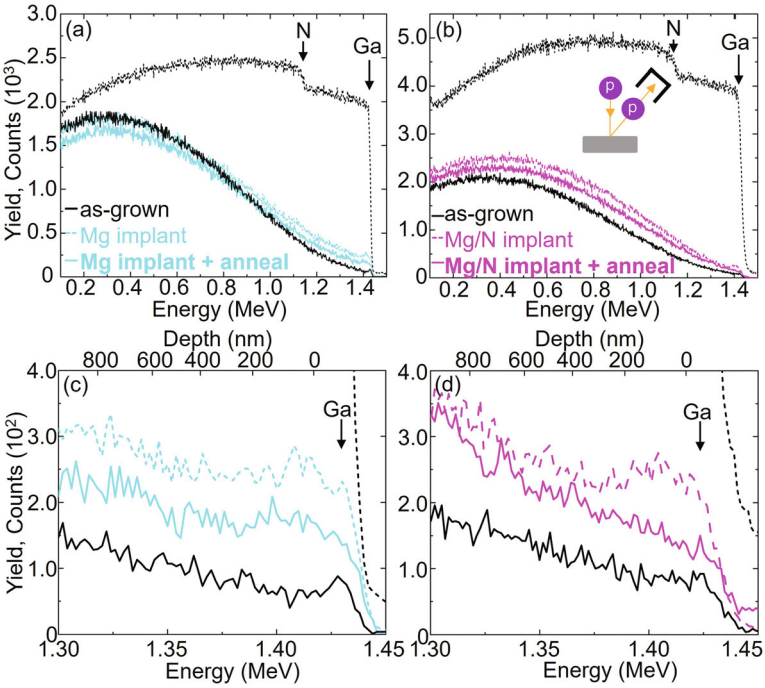

Fig. 20.13 (**a**) and (**b**) Random and channeling Rutherford backscattering spectrometry (RBS) spectra from p-GaN prepared by ion implantation plus gyrotron annealing, with close-up views of the RBS spectra in (**c**) and (**d**). The dashed and solid black spectra in (a)–(d) are random and channeling data from MOVPE-grown UID GaN prior to ion implantation (as-grown). The dashed and solid cyan spectra are channeling data following Mg implantation and Mg implantation + gyrotron annealing, respectively. Finally, the dashed and solid magenta spectra are channeling data following Mg/N co-implantation and Mg/N co-implantation plus gyrotron annealing. For both Mg implantation and Mg/N co-implantation, implantation increases the channeling backscattered yield, with a partial decrease following gyrotron annealing

Table 20.5 Crystallinity of the Mg-implanted and Mg/N co-implanted GaN, before and after gyrotron annealing: ratios of the channeling to random yields, summed over the top 100 nm, the so-called minimum yield, χ_{min}; the fraction of displaced Ga, N_d/N; minimum yield from angular yield scans, Y_{min}; half-angle at half-minimum of angular yield scans, $\psi_{1/2}$ (°); and lateral displacement of Ga atoms, r_x (nm). For this analysis, χ_{min} and $\psi_{1/2}$ for the as-grown GaN from Table 20.2 are defined as χ_0 and $\psi_{1/2}$, respectively

Implanted GaN	χ_{min}	N_d/N	Y_{min}	$\psi_{1/2}$ (°)	r_x (nm)
As-grown	0.018	0.009	N/A	N/A	N/A
Mg	0.058	0.049	N/A	N/A	N/A
Mg + gyrotron	0.041	0.032	N/A	N/A	N/A
As-grown	0.022	0.013	0.03	0.55	0.006
Mg/N	0.063	0.054	0.10	0.55	0.006
Mg/N + gyrotron	0.036	0.027	0.05	0.57	0.006

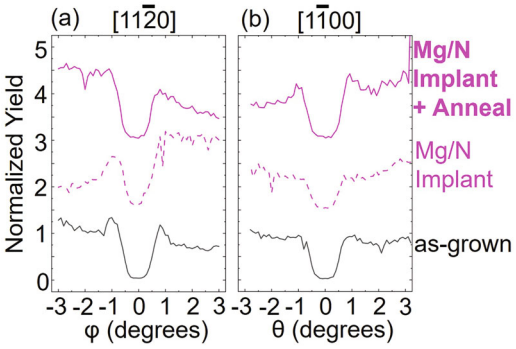

Fig. 20.14 Angular-dependence of the [0001] channeling Rutherford backscattering spectrometry (RBS/c) yields, rotated about the $[11\bar{2}0]$ and $[1\bar{1}00]$ axes, collected from the top 100 nm, for MOVPE-grown GaN prior to ion implantation (as-grown, black), following Mg/N co-implantation (magenta, dashed), and following Mg/N co-implantation plus gyrotron annealing (magenta, solid)

As shown in Table 20.5, for the as-grown UID GaN "reference" samples, $\chi_{min} = 0.020 \pm 0.002$, indicating a fraction of displaced Ga, $N_d/N = 0.011 \pm 0.002$. We note that the values of χ_{min} and N_d/N for these GaN reference samples are systematically higher than those of the as-grown GaN in Table 20.2, likely due to differences in the starting substrates and MOVPE-growth of the GaN layers.

For the Mg implanted GaN layers, the minimum yield increases to $\chi_{min} = 0.058$, indicating an increase in the fraction of displaced Ga to $N_d/N = 0.049$. Following gyrotron annealing, the crystallinity is partially recovered, with the channeling yield decreasing to $\chi_{min} = 0.041$, and the fraction of displaced Ga decreasing to $N_d/N = 0.032$.

When Mg and N are simultaneously implanted, the minimum yield increases further to $\chi_{min} = 0.063$, indicating an increase in the fraction of displaced Ga to $N_d/N = 0.054$. Interestingly, following gyrotron annealing, the crystallinity recovery is substantial, with the channeling yield decreasing to $\chi_{min} = 0.036$, and the fraction of displaced Ga decreasing to $N_d/N = 0.027$. These results support the hypothesis that the excess N provided by Mg/N co-implantation enhances recovery of crystallinity during gyrotron annealing.

The angular-dependence of the RBS/c yields are shown in Fig. 20.14 for (a) $Y_{Ga}(\phi)$ (rotating about the $[11\bar{2}0]$) and (b) $Y_{Ga}(\theta)$ (rotating about the $[1\bar{1}00]$). $Y_{Ga}(\theta)$ and $Y_{Ga}(\phi)$ were collected from the top 100 nm of the Mg/N co-implanted, Mg/N co-implanted plus gyrotron annealed, and as-grown GaN films. For the as-grown GaN, the $Y_{min,Ga}$ values are essentially identical for $Y_{Ga}(\theta)$ and $Y_{Ga}(\phi)$. For these data, shoulders are apparent near the channel edges for the as-grown Y_{ϕ}, presumably due to flux-focusing, as described earlier. The presence of well-defined shoulders suggests a highly crystalline structure, as evidenced by the low values of χ_{min} and N_d/N in Table 20.5.

As summarized in Table 20.5, $Y_{min} = 0.03$ for the as-grown GaN, similar to the values for MOVPE-grown GaN reported in Table 20.2. Following Mg/N

co-implantation, Y_{min} increases to 0.10, recovering to 0.05 following gyrotron annealing. $\psi_{1/2}$ values of 0.56 ± 0.01°are apparent for as-grown and Mg/N co-implanted GaN, consistent with earlier measurements of GaN [12, 15, 18]. The corresponding displacements of Ga atoms from the [0001] row, r_x, are 0.006 nm, similar to the thermal vibration amplitude. Since Mg/N co-implantation and gyrotron annealing have a minimal influence on the $\psi_{1/2}$ values, it is likely that those processes have not introduced impurities into the [0001] channels.

3.3 *Electric Field-Assisted Diffusion*

In this section, we present investigations of GaN structures prepared by an electric field-assisted diffusion process. Following a brief review of electric field-assisted diffusion and its potential impact on vertical GaN device technology, we describe the sequences of deposition and annealing used to prepare the structures. We then present RBS/c data, emphasizing the impact of the annealing and Mg diffusion processes on GaN crystallinity.

Selective solid-state diffusion of Mg into GaN [61, 62] has been suggested as an alternative approach to achieve vertical p-n devices. However, high concentrations of V_{Ga} are needed to facilitate Mg_{Ga} formation and diffusion. Typically, the high temperatures needed to produce V_{Ga} also lead to surface N loss and the formation of V_N. Recently, an alternative approach, based upon vacancy-assisted impurity diffusion (VAID) [63, 64], has been proposed for selective p-type doping of GaN with Mg [65]. In brief, the approach consists of deposition of a magnesium-containing insulator and a gallate-forming metal atop GaN, as shown in Fig. 20.15, for the combination of MgF_2 and gold. It is hypothesized that the band-bending introduced at the MgF_2/GaN interface lowers the GaN conduction band edge toward mid-gap, thereby lowering the formation energy of V_{Ga}. Furthermore, it is hypothesized that the built-in electric field provided by the metal (Au)-insulator (MgF_2)-semiconductor (GaN) structure enhances Mg diffusion into GaN.

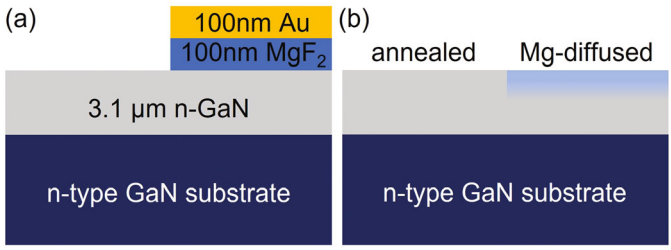

Fig. 20.15 Epitaxial n-GaN layers for studies of electric field-assisted Mg diffusion in GaN illustrated before and after heat-treatment: (**a**) a metallic bilayer consisting of 100 nm Au deposited on 100 nm MgF_2 was deposited through a shadow mask blocking half of a GaN layer and (**b**) following annealing for 50 min at 700, 800, or 900 °C, the structures consist of both "annealed" reference and "Mg-diffused" regions

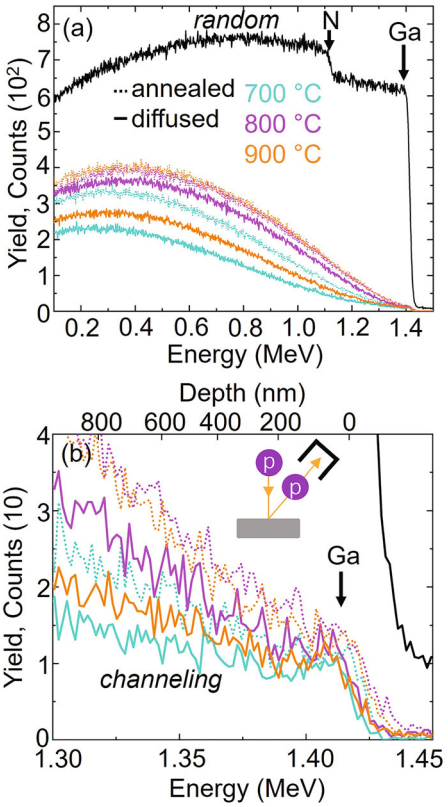

Fig. 20.16 (**a**) Random and channeling Rutherford backscattering spectrometry (RBS) spectra from GaN prepared by annealing to 700 °C (teal), 800 °C (purple), and 900 °C (orange), both with (solid) and without (dashed) Mg diffusion; close-up views of the RBS spectra are shown in (**b**). The black spectra in (a) and (b) correspond to representative random data, in this case for the 700 °C annealed reference GaN

For these investigations, a metallic bilayer consisting of 100 nm gold deposited onto 100 nm MgF_2 was deposited through a shadow mask blocking half of several Si-doped GaN layers, as illustrated in Fig. 20.15. Each structure was annealed in Ar_2 gas for 50 min at 700, 800, and 900 °C, forming both "annealed" reference and "Mg diffused" regions.

The [0001] channeling RBS spectra for annealed reference GaN (dashed) and Mg-diffused GaN (solid) are shown in Fig. 20.16a and b, with 700 °C (teal), 800 °C (purple), and 900 °C (orange). For comparison, a representative random spectrum, in this case from the 700 °C annealed reference GaN, is plotted in black. In Fig. 20.16a, a high backscattered yield, with well-defined N- and Ga-edges, is apparent for the random spectra, with significantly reduced yield for the channeling spectra, as expected for single crystals. The close-up view of the channeling spectra in Fig. 20.16b allow us to quantify changes in crystallinity, at specific depths, following annealing and Mg-diffusion.

Table 20.6 Crystallinity of the annealed reference and Mg-diffused GaN: ratios of the channeling to random yields, summed over the top 100 nm, the so-called minimum yield, χ_{min}; the fraction of displaced Ga, N_d/N; minimum yield from angular yield scans, Y_{min}; half-angle at half-minimum of angular yield scans, $\psi_{1/2}$ (°); and lateral displacement of Ga atoms, r_x (nm). For this analysis, χ_{min} and $\psi_{1/2}$ for the as-grown GaN from Table 20.2 are defined as χ_0 and $\psi_{1/2}$, respectively

Processing T (°C)	Mg Diffused?	χ_{min}	N_d/N	Y_{min}	$\psi_{1/2}$ (°)	r_x (nm)
700	N	0.019	0.010	0.01	0.58	0.006
700	Y	0.017	0.008	0.03	0.52	0.006
800	N	0.026	0.016	0.01	0.52	0.007
800	Y	0.021	0.011	0.01	0.53	0.007
900	N	0.025	0.015	0.02	0.54	0.007
900	Y	0.020	0.010	0.01	0.75	0.004

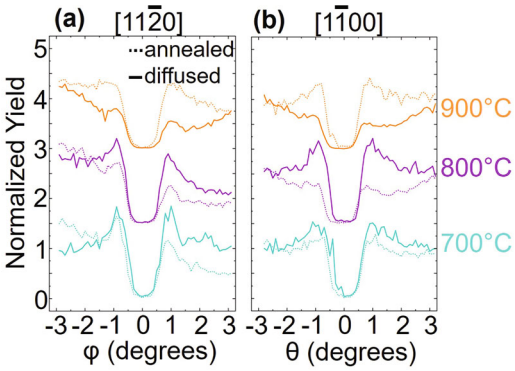

Fig. 20.17 Angular-dependence of the [0001] channeling Rutherford backscattering spectrometry (RBS/c) yields, rotated about the $[11\bar{2}0]$ and $[1\bar{1}00]$ axes, collected from the top 100 nm, for GaN annealed to 700 °C (teal), 800 °C (purple), and 900 °C (orange), both with (solid) and without (dashed) Mg diffusion

To quantify the depth-dependent crystallinity, we consider the fractions of backscattered ions using the minimum yield, χ_{min}, summed over the top 100 nm. As shown in Table 20.6, for the annealed reference layers, χ_{min} ranges from 0.019 to 0.026, indicating a fraction of displaced Ga, $N_d/N = 0.010–0.016$. We note that the values of χ_{min} and N_d/N for these annealed GaN reference layers are higher than those of the as-grown GaN in Table 20.2, presumably due to Ga and/or N loss at the surface during annealing. However, the χ_{min} and N_d/N are similar to those of the as-grown GaN in Table 20.5.

For the Mg-diffused regions, as shown in Table 20.6, χ_{min} ranges from 0.017 to 0.021, indicating a fraction of displaced Ga, $N_d/N = 0.008–0.011$. This decrease in χ_{min} and N_d/N for the Mg-diffused regions supports the hypothesis that MgF_2 has lowered the formation energy for V_{Ga}, enabling the formation and diffusion of Mg_{Ga}. It is worth noting that the 700 °C Mg-diffused GaN layer exhibits the lowest values of χ_{min} and N_d/N, with crystallinity similar to that of the continuous p-i-n GaN structure from Table 20.3.

The angular-dependence of the RBS/c yields are shown in Fig. 20.17a $Y_{Ga}(\phi)$ (rotating about the $[11\bar{2}0]$) and (b) $Y_{Ga}(\theta)$ (rotating about the $[1\bar{1}00]$). Spectra were

collected from the top 100 nm of the GaN layers prepared by annealing to 700 °C, 800 °C, and 900 °C, both with (solid) and without (dashed) Mg diffusion. For the 700 °C annealed reference and Mg-diffused GaN layers, the $Y_{min,Ga}$ values are essentially identical for $Y_{Ga}(\theta)$ and $Y_{Ga}(\phi)$. Furthermore, for the 700 °C Mg-diffused layers, well-defined shoulders are apparent near the channel edges for Y_{ϕ}, presumably due to flux-focusing, as described earlier. The presence of well-defined shoulders suggests a highly crystalline structure, as evidenced by the low values of χ_{min} and N_d/N in Table 20.6.

As summarized in Table 20.6, $Y_{min} \leq 0.03$ for all of the annealed references and Mg-diffused GaN regions is similar to the values reported for the as-grown and etched GaN structures discussed in Table 20.2. For processing temperatures of 700 and 800 °C, $\psi_{1/2}$ values of $0.55 \pm 0.03°$ are apparent—consistent with earlier measurements of GaN [12, 15, 18]. The corresponding displacements of Ga atoms from the [0001] channel, r_x, are 0.006–0.007 nm, similar to the thermal vibration amplitude. Since Mg-diffusion at 700 and 800 °C has a minimal influence on the $\psi_{1/2}$ values, it is likely that those processes have not introduced impurities into the [0001] channels. However, for the 900 °C Mg-diffused GaN regions, a substantial increase in $\psi_{1/2}$ and corresponding decrease in r_x are apparent. While the value of r_x is apparently lower than the thermal vibration amplitude for GaN, the increase in $\psi_{1/2}$ suggests that this process has effectively removed impurities from the [0001] channel, yielding Mg incorporated primarily as Mg_{Ga}. This finding is consistent with the reported achievement of hole conduction for the highest processing temperature (915 °C) for Au-assisted Mg diffusion [65].

4 Concluding Remarks

In this chapter, we described ion beam analysis techniques and their role in developing new understanding of relationships between structure, chemistry, and electronic states at GaN surfaces and interfaces intended for use in vertical GaN p-i-n devices. Following a description of the ion beam analysis and chemical and electronic characterization methods, we presented investigations of surface treatments for selective-area regrowth of GaN substrates and regrown epitaxial layers, as well as p-doped GaN layers prepared by Mg ion implantation plus gyrotron annealing and electric field-assisted Mg diffusion. In this section, we summarize the main findings and make suggestions for future opportunities.

For the surface-treated UID-GaN structures, the lowest fraction of near-surface atomic displacements and correspondingly most ideal diode characteristics are observed for the all in situ prepared GaN structures. Meanwhile, the highest fraction of near-surface atomic displacements—with correspondingly far from ideal diode characteristics—are apparent for the ICP-etched structures. Fortunately, the near-surface crystallinity and ideal diode characteristics are restored by subsequent TBCl etching.

For the GaN p-i-n structures, the fraction of displaced Ga atoms is nearly doubled, presumably due to the displacement of Ga by Mg incorporation in the p-type layers. Air exposure prior to p-type layer growth leads to elevated [Si] at the p-i regrowth interface, and ICP etching further enhances [Si], [H], and [Mg] at that interface. The resulting DAP emission intensity is reduced by the interfacial impurities, and YL emission is observed due to a surface state associated with air exposure.

For GaN structures prepared by Mg implantation and Mg/N co-implantation, subsequent gyrotron annealing provides partial recovery of crystallinity. Interestingly, the excess N provided by co-implantation enhances the crystallinity recovery during gyrotron annealing, with minimal introduction of impurities into the [0001] channels, presumably due to primarily substitutional Mg incorporation.

Finally, for GaN structures prepared by electric field-assisted Mg diffusion, we consider both the annealed reference and the Mg-diffused regions. Although the near-surface crystallinity is likely degraded by Ga and/or N loss at the surface during annealing, the Mg-diffused regions exhibit a substantial recovery of crystallinity, with near-surface atomic displacements comparable to those of the continuous GaN p-i-n structures prepared by MOVPE. For all annealing temperatures, the Mg-diffusion process has minimized the introduction of impurities into the [0001] channels, with 900 °C annealing apparently leading to the most effective substitutional Mg incorporation.

Looking to the future, these findings suggest that successful implementation of vertical p-n GaN devices may require hybrid approaches, such as localized Mg ion implantation and/or localized electric field-assisted Mg diffusion in combination with epitaxy [66]. For example, a stable focused ion beam (FIB) source for Mg was recently demonstrated [22], and plans are underway to integrate a FIB-based Mg source with molecular beam epitaxy in order to achieve both lateral and vertical selectivity in p-type doping of GaN.

For further insight into Mg dopant incorporation mechanisms and the interplay between structure, chemistry, and electronic states at GaN surfaces and interfaces, a combined experimental-computational approach is needed. In particular, we suggest using density functional theory (DFT) to generate relaxed structures of GaN crystals containing substitutional and/or interstitial impurities. These structures would then be used as input in combined Monte Carlo-molecular dynamics (MC-MD) ion channeling simulations of angular yield scans for comparison to experiment, as described in Refs [20, 67]. This combined experimental-computational approach will enable new understanding of dopant incorporation mechanisms and the influence of point defects on the properties of GaN surfaces and interfaces intended for use in vertical GaN p-i-n devices.

References

1. H. Nie, Q. Diduck, B. Alvarez, A.P. Edwards, B.M. Kayes, M. Zhang, G. Ye, T. Prunty, D. Bour, I.C. Kizilyalli, 1.5-kV and 2.2-mΩ -cm^2 Vertical GaN Tran-sistors on Bulk-GaN Substrates. IEEE Electron Device Lett. **35**(9), 939–941 (2014)
2. X. Liu, F. Lin, J. Li, Y. Lin, J. Wu, H. Wang, X. Li, S. Huang, Q. Wang, H.-C. Chiu, H.-C. Kuo, 1.7-kV vertical GaN-on-GaN Schottky barrier diodes with helium-implanted edge termination. IEEE Trans. Electron Devices **69**(4), 1938–1944 (2022)
3. Y. Zhang, M. Sun, Z. Liu, D. Piedra, H.-S. Lee, F. Gao, T. Fujishima, T. Palacios, Electrothermal simulation and thermal performance study of GaN vertical and lateral power transistors. IEEE Trans. Electron Devices **60**, 2224 (2013)
4. T. Pu, U. Younis, H.-C. Chiu, K. Xu, H.-C. Kuo, X. Liu, Review of recent progress on vertical GaN-based PN diodes. Nanoscale Res. Lett. **16**, 101 (2021)
5. G. Kipshidze, V. Kuryatkov, B. Borisov, Y. Kudryavtsev, R. Asomoza, S. Nikishin, H. Temkin, Mg and O codoping in p-type GaN and AlxGa1-xN (0<x <0.08). Appl. Phys. Lett. **80**, 2910 (2002)
6. S. Brochen, J. Brault, S. Chenot, A. Dussaigne, M. Leroux, B. Damilano, Dependence of the Mg-related acceptor ionization energy with the acceptor con- centration in p-type GaN layers grown by molecular beam epitaxy. Appl. Phys. Lett. **103**, 032102 (2013)
7. J.K. Sheu, G.C. Chi, The doping process and dopant characteristics of GaN. J. Phys. Condens. Matter **14**, R657 (2002)
8. B. McEwen, M.A. Reshchikov, E. Rocco, V. Meyers, K. Hogan, O. Adrieiev, M. Vorobiov, D.O. Demchenko, F. Shahedipour-Sandvik, MOCVD growth and characterization of Be-Doped GaN. ACS Appl. Electron. Mater. **4**, 3780 (2022)
9. J. Kennedy, A. Markwitz, H.J. Trodahl, B.J. Ruck, S.M. Durbin, W. Gao, Ion Beam analysis of amorphous and nanocrystalline group III-V nitride and ZnO thin films. J. Electron. Mater. **36**, 472 (2007)
10. K.L. Enisherlova, V.S. Kulikauskas, V.V. Zatekin, T.F. Rusak, N.B. Gladysheva, I.I. Razgulyaev, AlGaN/GaN heterostructure study using Rutherford backscattering spectrometry. J. Surf. Investig. X-Ray Synchrotron Neutron Tech. **5**, 626 (2011)
11. B. Sundaravel, E.Z. Luo, J.B. Xu, I.H. Wilson, W.K. Fong, L.S. Wang, C. Surya, Ion channeling studies on mixed phases formed in metalorganic chemical vapor deposition grown Mg-doped GaN on Al2O3(0001). J. Appl. Phys. **87**, 955 (2000)
12. M. Lind'en, R. Hellborg, Crystalline order and disorder in epitaxial GaN. Nucl. Instrum. Methods Phys. Res. B **68**, 170 (1992)
13. M. Usman, A. Hall'en, A. Nazir, Ion implantation induced nitrogen defects in GaN. J. Phys. D **48**, 455107 (2015)
14. B. Hollander, S. Mantl, M. Mayer, C. Kirchner, A. Pelzmann, M. Kamp, S. Christiansen, M. Albrecht, H.P. Strunk, Ion channeling studies of GaN layers on c-oriented sapphire. Nucl. Instrum. Methods Phys. Res. B **136**, 1248 (1998)
15. A. Turos, R. Ratajczak, K. Pagowska, A. Stonert, L. Nowicki, P. Caban, Nitrogen sublattice analysis in GaN by non-Rutherford He-ion scattering. Nucl. Instrum. Methods Phys. Res. B **266**, 1897 (2008)
16. S. Kurai, T. Saimei, M. Konishi, S. Kubo, T. Taguchi, *Identification of Homogenous and Inhomogenous Structures of NH_3 GS-MBE-Grown GaN Epilayers by Ion-Channeling Studies, in Compound Semiconductors 2001* (CRC Press, 2002)
17. N. Nishikata, K. Kushida, T. Nishimura, T. Mishima, K. Kuriyama, T. Nakamura, Evaluation of lattice displacement in Mg-implanted GaN by Rutherford backscattering spectroscopy. Nucl. Instrum. Methods Phys. Res. B **409**, 302 (2017)
18. A. Turos, L.J. Nowicki, A. Stonert, M. Leszczyn'ski, I. Grzegory, S. Porowski, Ion channeling study of GaN single crystals. Mater. Sci. Forum **248–249**, 419 (1997)
19. A. Redondo-Cubero, K. Lorenz, R. Gago, N. Franco, S. Fern´andez-Garrido, P.J.M. Smulders, E. Mun˜oz, E. Calleja, I.M. Watson, E. Alves, Breakdown of anomalous channeling with ion

energy for accurate strain determination in GaN-based heterostructures. Appl. Phys. Lett. **95**, 051921 (2009)
20. J.J.P. Cooper, T. Jen, A. Novak, Z. Xi, L. Qi, F.U. Naab, Y.Q. Wang, R.S. Goldman, Onset of tetrahedral interstitial formation in GaAsN alloys. Appl. Phys. Lett. **124**, 161108 (2024)
21. A. Chang, B. Li, S. Wang, S. Frisone, R. Goldman, J. Han, L. Lauhon, Unveiling the influence of selective-area-regrowth interfaces on local electronic properties of GaN p-n junctions for efficient power devices. Nano Energy **102**, 107689 (2022)
22. M. Titze, A. Katzenmeyer, S. Frisone, J.A. Ohlhausen, A. Flores, D. Campbell, B. Li, Y. Wang, J. Han, E.S. Bielejec, R.S. Goldman, Comparison of Mg-based liquid metal ion sources for scalable focused-ion-implantation doping of GaN. AIP Adv. **14**, 045326 (2024)
23. W.-K. Chu, J.W. Mayer, M.-A. Nicolet, Chapter 8 – Use of channeling techniques, in *Backscattering Spectrometry*, ed. by W.-K. Chu, J.W. Mayer, M.-A. Nicolet, (Academic Press, 1978), pp. 223–275
24. L.C. Feldman, J.W. Mayer, S.T. Picraux, Chapter 3 – Particle distributions within the channel, in *Materials Analysis by Ion Channeling*, ed. by L.C. Feldman, J.W. Mayer, S.T. Picraux, (Academic Press, San Diego, 1982), pp. 61–87
25. Y. Yamamura, W. Takeuchi, T. Kawamura, *The Screening Length of Interatomic Potential in Atomic Collisions*, vol No. 45 (National Institute for Fusion Science, 1998)
26. A. Yoshiasa, K. Koto, H. Maeda, T. Ishii, The mean-square relative displacement and displacement correlation functions in tetrahedrally and octahedrally coordinated A8B8-N crystals. Jpn. J. Appl. Phys. **36**, 781 (1997)
27. K. Kubota, T. Nishimura, K. Kuriyama, T. Nakamura, Evaluation of lattice displacement and electrical property of Zn-ion implanted GaN by Rutherford backscattering spectrometry. Nucl. Instrum. Methods Phys. Res. B **451**, 70 (2019)
28. K. Kunimune, Y. Soeda, S. Itami, K. Kikuta, Adhesive Polyimide Film, US5300627A (5 April 1994)
29. S. Damache, S. Djaroum, S. Ouichaoui, L. Amari, D. Moussa, Stopping powers and energy loss straggling for (0.9–3.4) MeV protons in a Kapton polyimide thin film. Nucl. Instrum. Methods Phys. Res. B **383**, 164 (2016)
30. M. Mayer, *SIMNRA User's Guide* (2020)
31. V. Quillet, F. Abel, M. Schott, Absolute cross section measurements for H and D elastic recoil using 1 to 2.5 MeV 4He ions, and for the 12C(d,p)13C and 16O(d,p1)17O nuclear reactions. Nucl. Instrum. Methods Phys. Res. B **83**, 47 (1993)
32. J.F. Ziegler, J.P. Biersack, The stopping and range of ions in matter, in *Treatise on Heavy-Ion Science: Volume 6: Astrophysics, Chemistry, and Condensed Matter*, ed. by D.A. Bromley, (Springer US, Boston, MA, 1985), pp. 93–129
33. M.L. Swanson, L. Shao, Ion Channeling, in *Handbook of Modern Ion Beam Materials Analysis, Second Edition*, (Materials Research Society, Warrendale, PA, 2009), pp. 247–284
34. D. Drouin, P. Hovington, R. Gauvin, CASINO: A new Monte Carlo code in C language for electron beam interactions. Scanning **19**, 20–28 (1997)
35. E.J. Gumbel, Le valeurs extr^emes des distributions statistiques. Annales de l'institut Henri Poincar'e **5**, 115 (1935)
36. W. Li, K. Nomoto, K. Lee, S.M. Islam, Z. Hu, M. Zhu, X. Gao, J. Xie, M. Pilla, D. Jena, H.G. Xing, Activation of buried P-GaN in MOCVD-regrown vertical structures. Appl. Phys. Lett. **113**, 062105 (2018)
37. J. Wang, L. Cao, J. Xie, E. Beam, R. McCarthy, C. Youtsey, P. Fay, High voltage, high current GaN-on-GaN p-n diodes with partially compensated edge termination. Appl. Phys. Lett. **113**, 023502 (2018)
38. K. Fu, H. Fu, X. Huang, H. Chen, T.-H. Yang, J. Montes, C. Yang, J. Zhou, Y. Zhao, Demonstration of 1.27 kV etch-then-regrow GaN p-n junctions with low leakage for GaN power electronics. IEEE Electron Device Lett. **40**, 1728 (2019)

39. C. Yang, H. Fu, V.N. Kumar, K. Fu, H. Liu, X. Huang, T.-H. Yang, H. Chen, J. Zhou, X. Deng, J. Montes, F.A. Ponce, D. Vasileska, Y. Zhao, GaN Vertical- Channel junction field-effect transistors with regrown p-GaN by MOCVD. IEEE Trans. Electron. Devices **67**, 3972 (2020)
40. J. Hu, Y. Zhang, M. Sun, D. Piedra, N. Chowdhury, T. Palacios, Materials and processing issues in vertical GaN power electronics. Mater. Sci. Semicond. Process. **78**, 75 (2018)
41. H. Fu, K. Fu, C. Yang, H. Liu, K.A. Hatch, P. Peri, D. Herath Mudiyanselage, B. Li, T.-H. Kim, S.R. Alugubelli, P.-Y. Su, D.C. Messina, X. Deng, C.-Y. Cheng, R. Vatan Meidanshahi, X. Huang, H. Chen, T.-H. Yang, J. Zhou, A.M. Armstrong, A.A. Allerman, E.T. Yu, J. Han, S.M. Goodnick, D.J. Smith, R.J. Nemanich, F.A. Ponce, Y. Zhao, Selective area regrowth and doping for vertical gallium nitride power devices: Materials challenges and recent progress. Mater. Today **49**, 296 (2021)
42. R.A. Ferreyra, B. Li, S. Wang, J. Han, Selective area doping of GaN toward high-power applications. J. Phys. D **56**, 373001 (2023)
43. K. Fu, H. Fu, X. Deng, P.-Y. Su, H. Liu, K. Hatch, C.-Y. Cheng, D. Messina, R.V. Meidanshahi, P. Peri, C. Yang, T.-H. Yang, J. Montes, J. Zhou, X. Qi, S.M. Goodnick, F.A. Ponce, D.J. Smith, R. Nemanich, Y. Zhao, The impact of interfacial Si contamination on GaN-on-GaN regrowth for high power vertical devices. Appl. Phys. Lett. **118**, 222104 (2021)
44. J. Hite, M.A. Mastro, Understanding interfaces for homoepitaxial GaN growth, in *Wide Bandgap Semiconductor-Based Electronics*, (IOP Publishing, 2020)
45. M. Noshin, R. Soman, X. Xu, S. Chowdhury, A systematic study of the regrown interface impurities in unintentionally doped Ga-polar c-plane GaN and methods to reduce the same. Semicond. Sci. Technol. **37**, 075018 (2022)
46. B. Li, S. Wang, M. Nami, J. Han, A study of damage-free in-situ etching of GaN in metalorganic chemical vapor deposition (MOCVD) by tertiarybutylchloride (TBCl). J. Cryst. Growth **534**, 125492 (2020)
47. P.-Y. Su, H. Liu, C. Yang, K. Fu, H. Fu, Y. Zhao, F.A. Ponce, Lateral and vertical growth of Mg-doped GaN on trench-patterned GaN films. Appl. Phys. Lett. **117**, 102110 (2020)
48. Y. Turkulets, N. Shauloff, O.H. Chaulker, Y. Shapira, R. Jelinek, I. Shalish, The GaN(0001) yellow-luminescence-related surface state and its interaction with air. Surf. Interfaces **38**, 102834 (2023)
49. D.N. Wijesundera, K.B. Ma, X.M. Wang, B.P. Tilakaratne, L. Shao, W.-K. Chu, The role of flux-focusing in the origin of shoulders in ion channeling angular scans. Phys. Lett. A **376**, 1763 (2012)
50. B. Paszkiewicz, R. Paszkiewicz, A. Szyszka, M. Wosko, W. Macherzynski, M. Tlaczala, R. Kudrawiec, M. Syperek, J. Misiewicz, E. Dumiszewska, W. Strupinski, Study of the activation process of Mg Dopant in GaN:Mg layers. Phys. Status Solidi C **3**, 579 (2006)
51. S. Huang, M. Ikeda, F. Zhang, M. Zhang, J. Zhu, S. Zhang, J. Liu, Achievable hole concentration at room temperature as a function of Mg concentration for MOCVD-grown p-GaN after sufficient annealing. J. Semicond. **45** (2024)
52. J.D. Greenlee, B.N. Feigelson, T.J. Anderson, J.K. Hite, K.D. Hobart, F.J. Kub, Symmetric multicycle rapid thermal annealing: Enhanced activation of implanted dopants in GaN. ECS J. Solid State Sci. Technol. **4**, 382 (2015)
53. T.J. Anderson, J.D. Greenlee, B.N. Feigelson, J.K. Hite, K.D. Hobart, F.J. Kub, Improvements in the annealing of mg ion implanted GaN and related devices. IEEE Trans. Semicond. Manuf. **29**, 343 (2016)
54. K. Hogan, S. Tozier, E. Rocco, I. Mahaboob, V. Meyers, B. McEwen, F. Shahedipour-Sandvik, R. Tompkins, M. Derenge, K. Jones, M. Shevelev, V. Sklyar, A. Lang, J. Hart, M. Taheri, M. Reshchikov, Novel Gyrotron Beam Annealing Method for Mg-Implanted Bulk GaN, in *2019 IEEE International Reliability Physics Symposium (IRPS)*, (2019), pp. 1–6
55. U. Singh, N. Kumar, A.K. Sinha, Gyrotron and its electron beam source: A review. J. Fusion Energ. **31**, 489 (2012)
56. V. Meyers, E. Rocco, T.J. Anderson, J.C. Gallagher, M.A. Ebrish, K. Jones, M. Derenge, M. Shevelev, V. Sklyar, K. Hogan, B. McEwen, F. Shahedipour- Sandvik, p-type conductivity

and damage recovery in implanted GaN annealed by rapid gyrotron microwave annealing. J. Appl. Phys. **128**, 085701 (2020)
57. K.T. Liu, Y.K. Su, S.J. Chang, Y. Horikoshi, Magnesium/nitrogen and beryllium/nitrogen coimplantation into GaN. J. Appl. Phys. **98**, 073702 (2005)
58. A. Uedono, R. Tanaka, S. Takashima, K. Ueno, M. Edo, K. Shima, K. Kojima, F. Chichibu, S. Ishibashi, Dopant activation process in Mg-implanted GaN studied by monoenergetic positron beam. Sci. Rep. **11**, 20660 (2021)
59. V. Meyers, E. Rocco, K. Hogan, B. McEwen, M. Shevelev, V. Sklyar, K. Jones, M. Derenge, F. Shahedipour-Sandvik, P-type conductivity and suppression of green luminescence in Mg/N co-implanted GaN by gyrotron microwave annealing. J. Appl. Phys. **130**, 085704 (2021)
60. V. Meyers, E. Rocco, B. McEwen, M. Shevelev, V. Sklyar, F. Shahedipour-Sandvik, Defect-mediated diffusion of implanted Mg in GaN: Suppressing dopant redistribution by sequential thermal and microwave annealing. J. Appl. Phys. **133**, 155701 (2023)
61. T. To, A.B. Djurisic, M.H. Xie, W.K. Fong, C. Surya, Doping of GaN by Mg Diffusion, in *2002 Conference on Optoelectronic and Microelectronic Materials and Devices. COMMAD 2002. Proceedings (Cat. No.02EX601)*, (2002), pp. 75–78
62. Y. Itoh, S. Lu, H. Watanabe, M. Deki, S. Nitta, Y. Honda, A. Tanaka, H. Amano, Substitutional diffusion of Mg into GaN from GaN/Mg mixture. Appl. Phys. Exp. **15**, 116505 (2022)
63. C.C. Tin, S. Mendis, M.T. Tin, T. Isaacs-Smith, J.R. Williams, A new approach in impurity doping of 4H-SiC using silicidation. J. Appl. Phys. **114**, 244502 (2013)
64. J.-H. Seo, H. Wu, S. Mikael, H. Mi, J.P. Blanchard, G. Venkataramanan, W. Zhou, S. Gong, D. Morgan, Z. Ma, Thermal diffusion boron doping of single-crystal natural diamond. J. Appl. Phys. **119**, 205703 (2016)
65. J.B. Varley, N.P. Allen, C. Frye, K.E. Kweon, V. Lordi, L. Voss, Field Assisted Interfacial Diffusion Doping through Heterostructure Design, US20210257463A1 (19 August 2021)
66. M.A. Briere, In-situ dopant implantation and growth of a III-nitride semiconductor body, US Patent 8.093,597 B2 (10 January 2012)
67. T. Jen, G. Vardar, Y.Q. Wang, R.S. Goldman, Identifying the dominant interstitial complex in dilute GaAsN alloys. Appl. Phys. Lett. **107**, 221904 (2015)